LETTERS
PUBLISHED ONLINE: 31 OCTOBER 2016 | DOI: 10.1038/NNANO.2016.214
nature nanotechnology

Helical edge states and fractional quantum Hall effect in a graphene electron–hole bilayer

Javier D. Sanchez-Yamagishi[1†], Jason Y. Luo[1†], Andrea F. Young[2], Benjamin M. Hunt[3], Kenji Watanabe[4], Takashi Taniguchi[4], Raymond C. Ashoori[1] and Pablo Jarillo-Herrero[1*]

Helical 1D electronic systems are a promising route towards realizing circuits of topological quantum states that exhibit non-Abelian statistics[1–4]. Here, we demonstrate a versatile platform to realize 1D systems made by combining quantum Hall (QH) edge states of opposite chiralities in a graphene electron–hole bilayer at moderate magnetic fields. Using this approach, we engineer helical 1D edge conductors where the counterpropagating modes are localized in separate electron and hole layers by a tunable electric field. These helical conductors exhibit strong non-local transport signals and suppressed backscattering due to the opposite spin polarizations of the counterpropagating modes. Unlike other approaches used for realizing helical states[5–7], the graphene electron–hole bilayer can be used to build new 1D systems incorporating fractional edge states[8,9]. Indeed, we are able to tune the bilayer devices into a regime hosting fractional and integer edge states of opposite chiralities, paving the way towards 1D helical conductors with fractional quantum statistics[10–13].

A helical 1D conductor is an unusual electronic system where forward and backward moving electrons have opposite spin polarizations. Theoretically, helical states can be realized by combining QH edge states with opposite spin and opposite chiralities[1,4]. Most experimental efforts though have focused on materials with strong spin–orbit coupling at zero magnetic field[5–7]. However, a QH edge state approach offers greater flexibility in system design with less dependence on material parameters. Moreover, a QH platform could harness the unique statistics of fractional QH states. Recent proposals have predicted that such a system, in the form of a fractional quantum spin Hall state, for example, could host fractional generalizations of Majorana bound states[10–13].

To simultaneously realize QH states with opposite chiralities, it is necessary to have coexisting electron-like and hole-like bands. Electron–hole QH states are observed in semi-metals, but suffer from low hole-mobilities[14,15]. In this respect, graphene is attractive because it has high carrier mobilities and electron–hole symmetry. In fact, the graphene electron and hole bands can be inverted by the Zeeman effect to realize helical states[16,17], but requires very large magnetic fields[18,19]. A similar outcome could be realized more easily in a bilayer system, where electric fields can dope one layer into the electron band and the other into the hole band. At moderate magnetic fields, this electron–hole bilayer will develop QH edge states with opposite chiralities in each layer. Note that unlike edge states in a lateral quantum Hall p–n junction[20], the electron–hole bilayer boundary will host modes that are counter-propagating and spaced apart by subnanometre distances. Here, we demonstrate such a graphene electron–hole bilayer, which we use to realize a helical 1D conductor made from QH edge states.

The studied devices consist of two monolayer graphene flakes that are stacked with a relative twist misalignment (Fig. 1a,b). The twist causes a low-energy decoupling of the layers, despite their tiny 0.34-nm interlayer spacing[21,22], that allows each layer to develop independent edge states in a magnetic field[22–25] (Fig. 1c). We fabricate a dual-gated structure where top and bottom gates allow us to control the total charge density of the twisted bilayer and the interlayer electric field (Fig. 1b). We define the total applied electron density as $n_{tot} = (C_T V_T + C_B V_B)/e$, where C_T and C_B are the top and bottom gate capacitances per unit area, V_T and V_B are the top and bottom gate voltages, and e is the electron charge. In a magnetic field, B, we consider the total filling factor $\nu_{tot} = n_{tot}(h/e)/B$, which is the number of filled Landau levels (h/e is the magnetic flux quantum, where h is Planck's constant). Applying antisymmetric gate voltages will impose an interlayer electric field that shifts charges between layers, causing them to have different filling factors. We present this experimental knob as the applied displacement field $D = (C_T V_T - C_B V_B)/2$ divided by the vacuum permittivity ε_0.

To establish the degree of interlayer coupling in our devices, we begin by measuring the QH effect. The QH effect is a sensitive probe of electron degeneracy and the underlying symmetries of the Landau levels; as such, the graphene QH effect is different for monolayers[26,27], AB-stacked bilayers[28] and twisted bilayers[23–25,29]. Figure 1d shows a two-probe conductance measurement, G, as a function of ν_{tot} in a twisted bilayer device at $B = 1$ T. The filling factors of the top and bottom layers are equal during the measurement ($\nu_{top} = \nu_{bottom} = \nu_{tot}/2$, $D = 0$), resulting in a QH plateau sequence double that of monolayer graphene due to the layer degeneracy. This sequence demonstrates that a large twist misalignment leads to a weak interlayer coupling that does not split the layer degeneracy, and therefore the system can be modelled as two monolayer graphene sheets conducting in parallel[29,30].

In low-disorder samples, electron exchange interactions break the graphene spin–valley degeneracy, leading to QH ferromagnetism[31–33]. We observe such degeneracy breaking at higher fields as a sequence of plateaus at all integer multiples of e^2/h from −4 to 4 ($B = 4$ T; Fig. 1e). This can be explained by exchange-driven breaking of spin–valley symmetry in each of the graphene layers, combined with the effects of the displacement field. For example, at $\nu_{tot} = 0$, both layers are charge neutral and we observe an insulating state ($G = 0$), similar to the exchange-driven insulating state observed in neutral monolayer graphene[19,32,33].

Decreasing ν_{tot} from 0 to −1, a small applied displacement field causes charge to be removed from the top layer preferentially. The result is a transition to a 1 e^2/h plateau, which we explain as conduction through a hole-like edge state in the top layer while the bottom layer

[1]Department of Physics, Massachusetts Institute of Technology, Cambridge, Massachusetts 02139, USA. [2]Department of Physics, University of California Santa Barbara, Santa Barbara, California 93106, USA. [3]Department of Physics, Carnegie Mellon University, Pittsburg, Pennsylvania 15213, USA. [4]Advanced Materials Laboratory, National Institute for Materials Science, Tsukuba, Ibaraki 305-0044, Japan. †These authors contributed equally to this work.
*e-mail: pjarillo@mit.edu

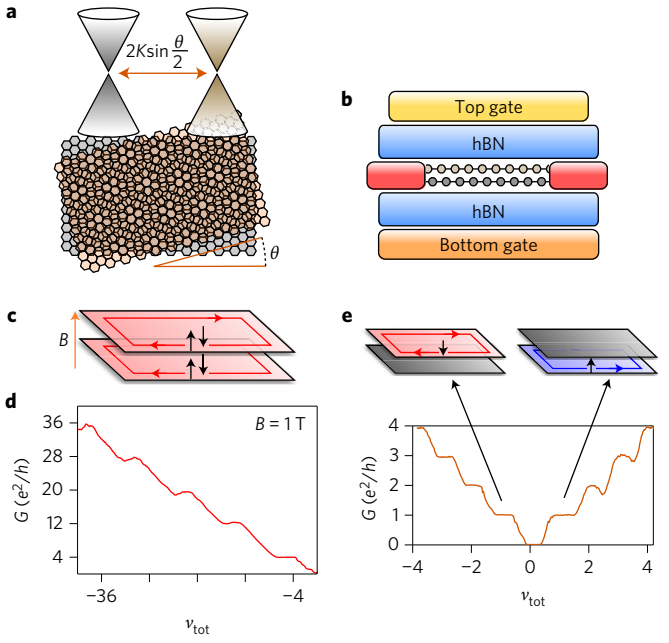

Figure 1 | Quantum Hall effect in twisted bilayer graphene with broken-symmetry states. a, Stacking two graphene layers with a relative twist angle θ decouples the Dirac cones from each layer via a large momentum mismatch ($K = 4\pi/3a$, where a is the graphene lattice constant). In a magnetic field, each layer will develop monolayer graphene-like Landau levels despite the tiny 0.34-nm interlayer spacing. **b**, Device schematic of twisted bilayer graphene encapsulated in hexagonal boron nitride (hBN) with dual gates. Contact electrodes are depicted in red. **c**, Cartoon of twisted bilayer QH edge states when both layers are at filling factor -2. Each layer has a spin degenerate edge state with a hole-like chirality (direction of chirality indicated by horizontal arrows). **d**, Two-probe conductance of a twisted bilayer graphene device at $B = 1$ T as a function of ν_{tot}. The sequence is exactly double the monolayer graphene sequence of $(2,6,10,14,\ldots)e^2/h$ (refs 26,27). A contact resistance has been subtracted to fit the $\nu_{tot} = -4$ plateau to 4 e^2/h. **e**, Two-probe conductance of the same device at $B = 4$ T showing broken-symmetry states. Contact resistances have been subtracted from the negative and positive ν_{tot} sides of the data. Note that this trace is taken with a small interlayer displacement field in order to observe all integer steps (see colour map in Fig. 2e). Cartoons depict proposed edge state configurations in the (0,–1) and (+1,0) states.

remains insulating (Fig. 1e, left cartoon). Conversely, increasing ν_{tot} to 1 preferentially adds charges to the bottom layer, resulting in an electron-like edge state with conductance of 1 e^2/h (Fig. 1e, right cartoon). We label these states by the filling factors on each layer as $(\nu_{bottom}, \nu_{top}) = (0,-1)$ and $(1,0)$. In monolayer graphene, the filling factor $\nu = \pm 1$ states are thought to be spin polarized due to the combined effects of Zeeman and QH ferromagnetism[20,33]. At $\nu = 1$, the spin magnetic moment is aligned with the magnetic field; for the hole-like $\nu = -1$ edge state, the spin is flipped since it originates from the bulk excited state. If the same effect occurs in twisted bilayer graphene, it should be possible to create a pair of helical edge states with opposite chiralities and opposite spin polarizations by realizing coexisting $\nu = 1$ and $\nu = -1$ states.

We now explore the outcomes when the twisted bilayer is electron–hole doped such that the layers have edge states of opposite chiralities. Starting with each layer in the insulating state at charge neutrality (0,0), we imbalance the bilayer with a displacement field such that the charge density from each layer is of equal magnitude but of opposite sign ($\nu_{top} = -\nu_{bottom}$, $\nu_{tot} = 0$; Fig. 2a). As the displacement field increases, the system first transitions to a conductive state of order e^2/h, and then transitions sharply to another insulating state at higher displacement fields (Fig. 2b,c). Assuming that transitions correspond to layer filling factor changes, we assign the conductive states to the $(\pm1,\mp1)$ charge configurations, and the insulating states at higher D magnitudes to the $(\pm2,\mp2)$ states. We have consistently observed this conductance sequence in all large-twist bilayer graphene devices that display broken-symmetry states (9 devices in total), with $(\pm1,\mp1)$ state conductances varying from 0.8 to 1.5 e^2/h.

To verify the assignment of the $(\pm1,\mp1)$ states, we studied a wider range of edge state configurations away from $\nu_{tot} = 0$. Figure 2d shows the two-probe conductance as a function of ν_{tot} and displacement field. The $(\pm1,\mp1)$ states form clearly defined plateaus in the map (white dotted circles). We model the sequence by considering all possible combinations of filling factors in the graphene zeroth Landau level with broken spin–valley degeneracy. The resulting map in Fig. 2e matches the entire sequence of plateau transitions observed in the two-probe conductance (Fig. 2d) and four-probe longitudinal resistance measurements (Supplementary Fig. 1). Furthermore, capacitance measurements on a different sample reveal that the bulk is insulating for all plateaus in the map, as expected for QH states (Supplementary Fig. 2). The consistency of the model with the observed plateaus supports the assignment of the conductive $\nu_{tot} = 0$ states to the $(\pm1,\mp1)$ filling factor configurations.

The measured conductances of nearly all the filling factor configurations are given by $G = \nu_{tot}\, e^2/h$. Noticeably, only the $(\pm1,\mp1)$ states depart from this pattern. When ν_{bottom} and ν_{top} have the same sign, this formula follows directly from the parallel conductance contributions of QH edge states in each layer. But for electron–hole bilayer combinations, such as the (+2,–2) or (+2,–1) states, this equation implies that conductance contributions from each layer can cancel. For this to occur, there must be a backscattering process that couples opposite chirality edge states between layers (Fig. 2a, bottom)[29]. Moreover, temperature dependence of the insulating $G = 0$ $(\pm2,\mp2)$ states suggests that this backscattering leads to a complete transport gap (Supplementary Fig. 5). Interlayer backscattering requires tunnelling between the closely spaced layers, which may be enhanced at the edge even if it is suppressed in the bulk. In contrast, the same backscattering process is nearly absent in the $(\pm1,\mp1)$ states, resulting in a conductive plateau of order e^2/h for a device with greater than 5-μm-long edges.

We also show that the $(\pm1,\mp1)$ states conduct through counterpropagating edge modes by measuring the non-local voltage response in the same device. In the non-local measurement, a voltage V_{NL} is measured between adjacent contacts far away from the electrodes where a current I_M is sourced and drained. We find that the non-local resistance $R_{NL} = V_{NL}/I_M$ of the $(\pm1,\mp1)$ states is 10 to 1,000 times larger than the resistance of other conductive states (Fig. 3c, white dotted regions and Fig. 3d). This non-local signal sharply differentiates the $(\pm1,\mp1)$ states from being either normal chiral edge states or diffusive conductors: the voltage drop along a chiral edge state is zero, while in a diffusive bulk conductor the non-local voltage far away from the source–drain electrodes is exponentially suppressed. In contrast to a weak bulk response, the strong non-local resistance of the $(\pm1,\mp1)$ states signifies that current flows predominately along the edge, with both forward and backward propagating modes equilibrating at the electrodes to give a voltage drop.

Based on the transport data collected—the mapping of the QH plateau sequence and the edge state non-local signal—we conclude that at filling factors $(\pm1,\mp1)$ conduction occurs through a pair of QH edge states with opposite chiralities (Fig. 2a, middle). Backscattering between the two counterpropagating modes is strongly suppressed, resulting in a highly conductive 1D transport channel with conductance ranging from 0.8 to 1.5 e^2/h for devices of different edge lengths (0.2–16 μm) (details in Supplementary Fig. 9). This is contrasted with the spin-degenerate $(\pm2,\mp2)$ states, where interlayer tunnelling leads to insulating behaviour in the

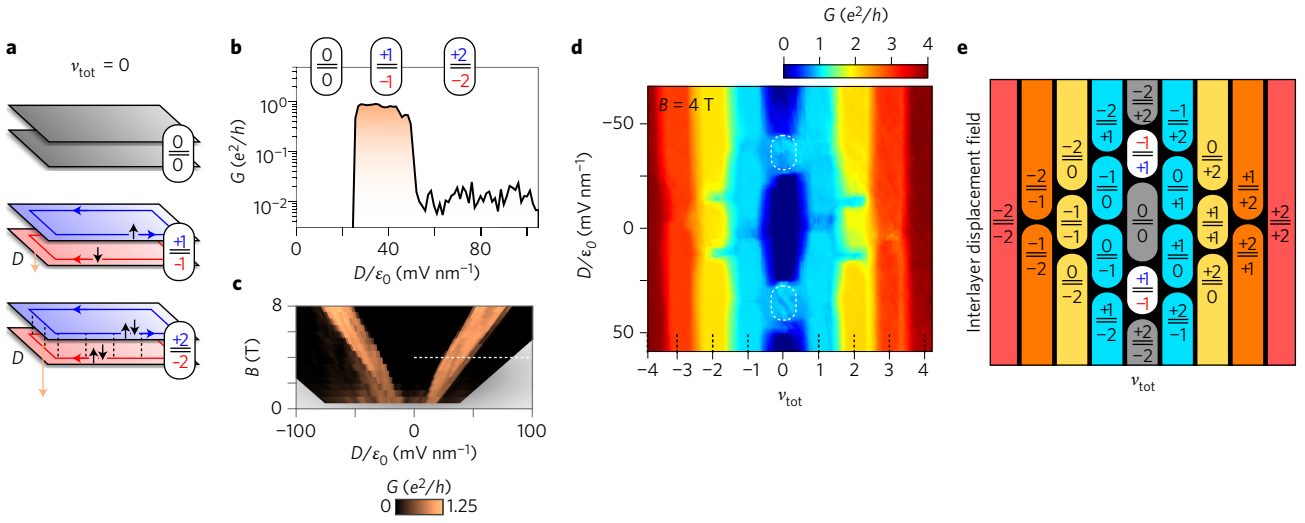

Figure 2 | Transport in graphene electron–hole bilayers. a, Cartoons depicting edge state configurations with $\nu_{top} = -\nu_{bottom}$. **b**, Measured two-probe conductance G for $\nu_{tot} = 0$ as a function of displacement field, D, at $B = 4$ T. The (–1,+1) state is conductive while the (–2,+2) state is insulating. **c**, Magnetic field dependence of $\nu_{tot} = 0$ line (white dashed line shows the location of the line trace in **b**). **d**, Two-probe conductance map, G, as function of ν_{tot} and D. Conductance is given by $\nu_{tot}(e^2/h)$ for all configurations except for the (±1,∓1) states (indicated by the dashed white circles). Contact resistances have been subtracted from the positive and negatives sides of the data to fit the $\nu_{tot} = \pm 1$ plateaus. **e**, Schematic map of possible filling factor combinations.

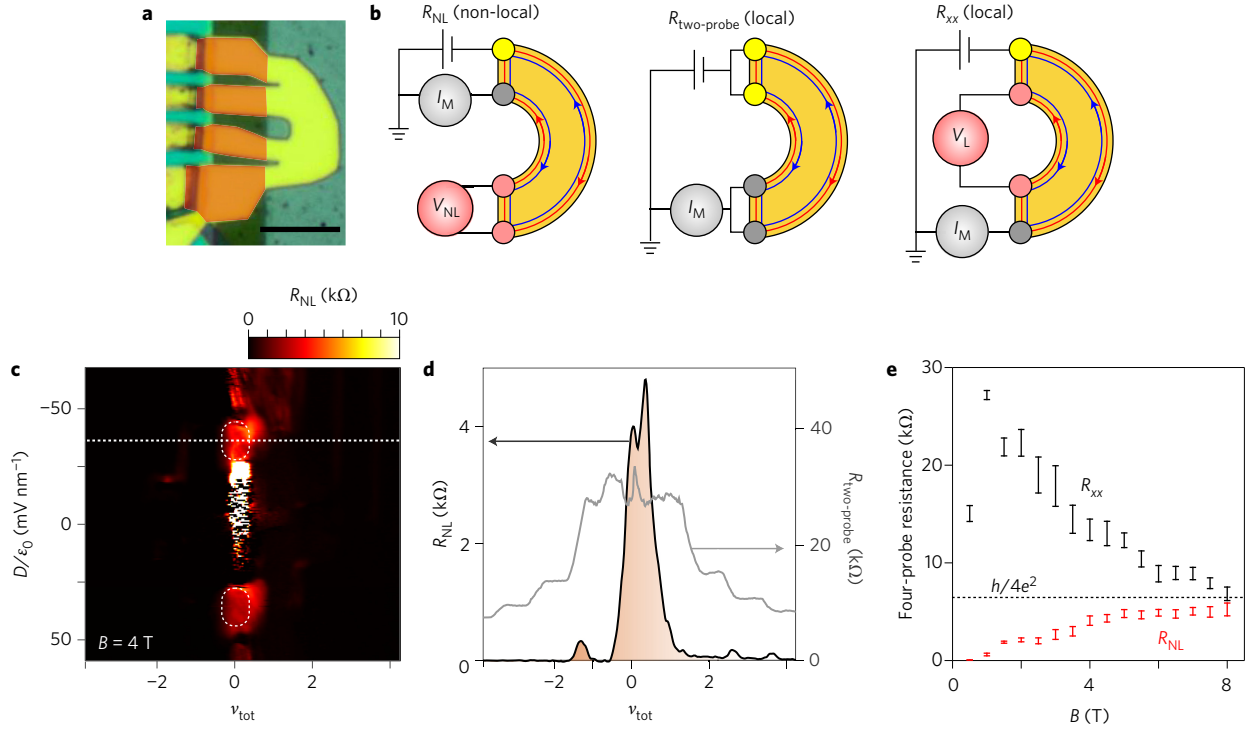

Figure 3 | Non-local measurements of helical edge states. a, Optical image of four-probe device. Scale bar, 5 μm. Graphite leads are highlighted in orange and the gold top-gate that covers the device is highlighted in yellow. **b**, Schematics of different measurement configurations for the four-probe device. **c**, Non-local resistance, R_{NL}, as a function of ν_{tot} and displacement field, D, measured at $B = 4$T. Dashed white circles highlight the (±1,∓1) states that exhibit a strong non-local signal, indicating transport through highly conductive counterpropagating edge modes. Axis ranges are identical to those in Fig. 2d. In the (0,0) insulating state, R_{NL} fluctuates strongly due to low current signals near the noise limit (bright white features). **d**, R_{NL} (black line, left axis) compared to two-probe resistance, $R_{two\text{-}probe}$, (grey line, right axis) of a constant D line cut through the (+1,–1) state (horizontal dashed line in Fig. 3c). R_{NL} is near zero when $R_{two\text{-}probe}$ exhibits a conductance plateau, since the voltage drop along a chiral edge state is zero. During plateau transitions, the bulk becomes conductive, resulting in a small peak that is suppressed by the non-local geometry of the measurement. **e**, Magnetic field dependence of R_{NL} and R_{xx} in the (+1,–1) state. Plotted points are determined by averaging the resistance over the region in the ν_{tot} and D map corresponding to the (+1,–1) state (error bars represent one standard deviation from the mean).

same devices (Fig. 2a). A simple explanation for the difference is that the counterpropagating modes of the (±1,∓1) states have opposite spin polarizations, which are the expected Zeeman plus exchange-driven ground states for monolayer graphene at $\nu = \pm 1$ (refs 20,33). When the spin wavefunctions on each layer are orthogonal, interlayer tunnelling processes are forbidden and the edge states are protected from

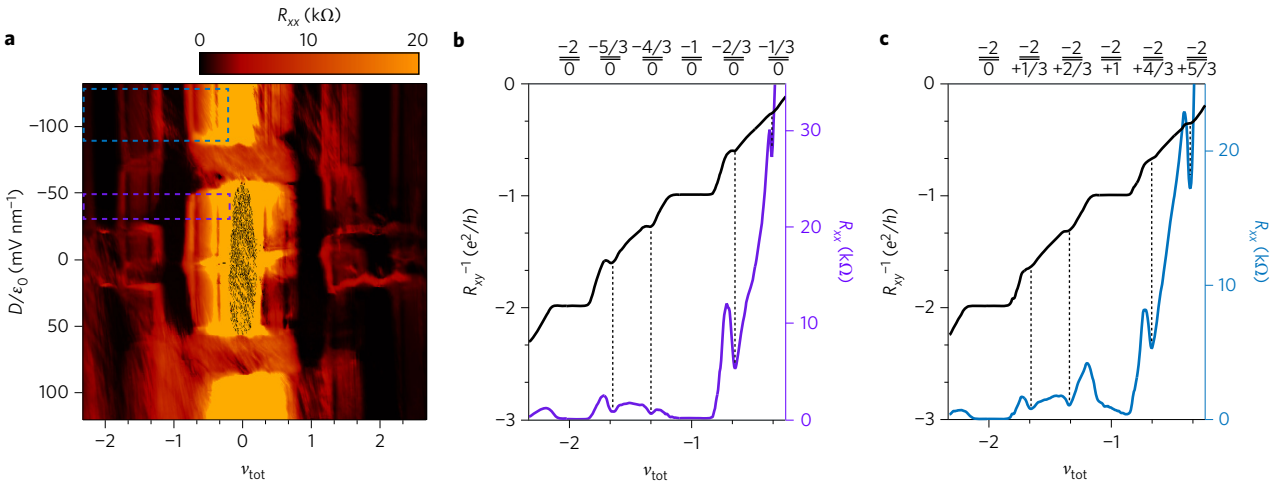

Figure 4 | Fractional QH effect in twisted bilayer graphene. a, R_{xx} measurements at $B = 9$ T as a function of ν_{tot} and D show clear minima at fractional values of $\nu_{tot} = \pm 1/3, \pm 2/3, \pm 4/3$ and $\pm 5/3$ indicating fractional quantum Hall states. Some electron–hole regions are obscured by contact-resistance effects at high fields. **b**,**c**, Comparison of R_{xx} and R_{xy} line cuts showing the bilayer fractional quantum Hall effect. R_{xx} minima at fractional values of ν_{tot} line up with plateaus in the measurement of $1/R_{xy}$. The plotted lines in **b** and **c** are averages of the measured quantities over a range of D field values as indicated respectively by the purple and blue rectangles in the colourmap of **a**. For the line trace in **b**, measurements correspond to fractional states in the top layer and an insulating $\nu = 0$ state in the bottom layer. For **c**, data correspond to electron–hole combinations.

backscattering. The result is a pair of helical edge states in the (±1,∓1) electron–hole bilayer.

The expected conductance of the helical edge states is $2\,e^2/h$ when backscattering is completely suppressed (each edge contributes $1\,e^2/h$ in parallel). In our two-probe measurements, we identify a significant reduction in the conductance due to contact resistances from the electrode/edge state interfaces (see Supplementary Materials). To avoid this effect, we measure the four-probe resistance of the (+1, −1) states as a function of magnetic field in both local (R_{xx}) and non-local configurations (R_{NL}) (Fig. 3e). Above 1.5 T, R_{NL} increases slowly until it saturates at high fields, while R_{xx} decreases to approach a similar value, despite the two measurements probing edges of very different lengths. Moreover, the measurements approach $h/4e^2$—the expected value for ballistic counterpropagating edge states that fully equilibrate at the contacts. The convergence of R_{xx} and R_{NL} suggests that backscattering in the helical (±1,∓1) states decreases steadily to zero with increasing magnetic field, resulting in a length-independent edge segment resistance of h/e^2.

We next examined the low-field regime of the (±1,∓1) states (Fig. 3e). At zero magnetic field, the non-local resistance is insignificant (1–10 Ω); as the magnetic field rises to 1.5 T, R_{NL} sharply increases by a factor of 100. This coincides with the emergence of clearly distinguished plateaus at (±1,∓1) in both the R_{NL} and $R_{two\text{-}probe}$ maps (Supplementary Fig. 10). We interpret the sharp increase in R_{NL} as the onset of conduction in the helical edge states at 1.5 T, a comparatively low field that is encouraging for future efforts to engineer topological superconductivity in this helical conductor[1,4].

One unique advantage of building a helical 1D conductor from QH edge states is the possibility of extending the system to fractional edge states[8,9]. As a promising step in this direction, we have observed the fractional QH effect in our high-quality devices. Figure 4a shows an R_{xx} measurement taken at $B = 9$ T, where clear minima are observed at fractional values of $\nu_{tot} = \pm 1/3, \pm 2/3, \pm 4/3$ and $\pm 5/3$. Simultaneous with the R_{xx} minima, we observed plateaus in $1/R_{xy}$ Hall measurements (Fig. 4b,c). From the location of the line cuts in Fig. 4b, we deduced that one layer is in the $\nu = 0$ insulating state, while the other layer hosts a fractional edge state. Interestingly, we also observed fractional states in the electron–hole bilayer regime (Fig. 4c), with clear fractional QH states that we identify with the (+1/3,−2), (+2/3,−2), (+4/3,−2) and (+5/3,−2) states. The Hall measurements follow $1/R_{xy} = \nu_{tot}e^2/h$, suggesting again the role of interlayer tunnelling, in this case resulting in coupling and complete backscattering between fractional and integer edge states on different layers. These observations of fractional QH states pave the way towards realizing a fractional quantum spin Hall state—a key ingredient in recent proposals to construct fractional generalizations of Majorana fermions[10–12].

Methods

Methods and any associated references are available in the online version of the paper.

Received 17 May 2016; accepted 13 September 2016; published online 31 October 2016

References

1. Qi, X.-L. & Zhang, S.-C. Topological insulators and superconductors. *Rev. Mod. Phys.* **83,** 1057–1110 (2011).
2. Lutchyn, R. M., Sau, J. D. & Das Sarma, S. Majorana fermions and a topological phase transition in semiconductor-superconductor heterostructures. *Phys. Rev. Lett.* **105,** 077001 (2010).
3. Oreg, Y., Refael, G. & von Oppen, F. Helical liquids and Majorana bound states in quantum wires. *Phys. Rev. Lett.* **105,** 177002 (2010).
4. Hasan, M. Z. & Kane, C. L. Colloquium: topological insulators. *Rev. Mod. Phys.* **82,** 3045–3067 (2010).
5. Konig, M. *et al.* Quantum spin Hall insulator state in HgTe quantum wells. *Science* **318,** 766–770 (2007).
6. Knez, I., Du, R.-R. & Sullivan, G. Evidence for helical edge modes in inverted InAs/GaSb quantum wells. *Phys. Rev. Lett.* **107,** 136603 (2011).
7. Mourik, V. *et al.* Signatures of Majorana fermions in hybrid superconductor-semiconductor nanowire devices. *Science* **336,** 1003–1007 (2012).
8. Bolotin, K. I., Ghahari, F., Shulman, M. D., Stormer, H. L. & Kim, P. Observation of the fractional quantum Hall effect in graphene. *Nature* **462,** 196–199 (2009).
9. Du, X., Skachko, I., Duerr, F., Luican, A. & Andrei, E. Y. Fractional quantum Hall effect and insulating phase of Dirac electrons in graphene. *Nature* **462,** 192–195 (2009).
10. Lindner, N. H., Berg, E., Refael, G. & Stern, A. Fractionalizing Majorana fermions: non-Abelian statistics on the edges of Abelian quantum Hall states. *Phys. Rev. X* **2,** 041002 (2012).
11. Cheng, M. Superconducting proximity effect on the edge of fractional topological insulators. *Phys. Rev. B* **86,** 195126 (2012).
12. Clarke, D. J., Alicea, J. & Shtengel, K. Exotic non-Abelian anyons from conventional fractional quantum Hall states. *Nat. Commun.* **4,** 1348 (2013).
13. Barkeshli, M. & Qi, X.-L. Synthetic topological qubits in conventional bilayer quantum Hall systems. *Phys. Rev. X* **4,** 041035 (2014).

14. Gusev, G. M. *et al.* Nonlocal transport near charge neutrality point in a two-dimensional electron-hole system. *Phys. Rev. Lett.* **108,** 226804 (2012).
15. Nichele, F. *et al.* Insulating state and giant nonlocal response in an InAs/GaSb quantum well in the quantum Hall regime. *Phys. Rev. Lett.* **112,** 036802 (2014).
16. Abanin, D. A., Lee, P. A. & Levitov, L. S. Spin-filtered edge states and quantum Hall effect in graphene. *Phys. Rev. Lett.* **96,** 176803 (2006).
17. Fertig, H. A. & Brey, L. Luttinger liquid at the edge of undoped graphene in a strong magnetic field. *Phys. Rev. Lett.* **97,** 116805 (2006).
18. Maher, P. *et al.* Evidence for a spin phase transition at charge neutrality in bilayer graphene. *Nat. Phys.* **9,** 154–158 (2013).
19. Young, A. F. *et al.* Tunable symmetry breaking and helical edge transport in a graphene quantum spin Hall state. *Nature* **505,** 528–532 (2014).
20. Amet, F., Williams, J. R., Watanabe, K., Taniguchi, T. & Goldhaber-Gordon, D. Selective equilibration of spin-polarized quantum Hall edge states in graphene. *Phys. Rev. Lett.* **112,** 196601 (2014).
21. Lopes dos Santos, J. M. B., Peres, N. M. R. & Castro Neto, A. H. Graphene bilayer with a twist: electronic structure. *Phys. Rev. Lett.* **99,** 256802 (2007).
22. Luican, A. *et al.* Single-layer behavior and its breakdown in twisted graphene layers. *Phys. Rev. Lett.* **106,** 126802 (2011).
23. de Gail, R., Goerbig, M. O., Guinea, F., Montambaux, G. & Castro Neto, A. H. Topologically protected zero modes in twisted bilayer graphene. *Phys. Rev. B* **84,** 045436 (2011).
24. Choi, M.-Y., Hyun, Y.-H. & Kim, Y. Angle dependence of the Landau level spectrum in twisted bilayer graphene. *Phys. Rev. B* **84,** 195437 (2011).
25. Moon, P. & Koshino, M. Energy spectrum and quantum Hall effect in twisted bilayer graphene. *Phys. Rev. B* **85,** 195458 (2012).
26. Zhang, Y., Tan, Y.-W., Stormer, H. L. & Kim, P. Experimental observation of the quantum Hall effect and Berry's phase in graphene. *Nature* **438,** 201–204 (2005).
27. Novoselov, K. S. *et al.* Two-dimensional gas of massless Dirac fermions in graphene. *Nature* **438,** 197–200 (2005).
28. Novoselov, K. S. *et al.* Unconventional quantum Hall effect and Berry's phase of 2π in bilayer graphene. *Nat. Phys.* **2,** 177–180 (2006).
29. Sanchez-Yamagishi, J. D. *et al.* Quantum Hall effect, screening, and layer-polarized insulating states in twisted bilayer graphene. *Phys. Rev. Lett.* **108,** 076601 (2012).
30. Schmidt, H., Lüdtke, T., Barthold, P. & Haug, R. J. Mobilities and scattering times in decoupled graphene monolayers. *Phys. Rev. B* **81,** 121403(R) (2010).
31. Zhang, Y. *et al.* Landau-level splitting in graphene in high magnetic fields. *Phys. Rev. Lett.* **96,** 136806 (2006).
32. Checkelsky, J. G., Li, L. & Ong, N. P. Zero-energy state in graphene in a high magnetic field. *Phys. Rev. Lett.* **100,** 206801 (2008).
33. Young, A. F. *et al.* Spin and valley quantum Hall ferromagnetism in graphene. *Nat. Phys.* **8,** 550–556 (2012).

Acknowledgements

We acknowledge helpful discussions with A. Stern, L. Levitov, L. Fu and V. Fatemi. We also acknowledge fabrication help from D. Wei, G. H. Lee, S. H. Choi and Y. Cao. This work has been primarily supported by the National Science Foundation (NSF) (DMR-1405221) for device fabrication, transport and data analysis (J.D.S.-Y., J.Y.L., P.J.-H.), with additional support from the National Science Scholarship Program, Singapore (J.Y.L.). This research has been funded in part by the Gordon and Betty Moore Foundation's EPiQS Initiative through Grant GBMF4541 to P.J.-H. The capacitance measurements have been supported in part by the Gordon and Betty Moore Foundation Grant GBMF2931 to R.C.A. and by the Science and Technology Center for Integrated Quantum Materials, NSF Grant (DMR-1231319) (A.F.Y., B.M.H. and R.C.A.). This work made use of the Materials Research Science and Engineering Center Shared Experimental Facilities supported by the NSF (DMR-0819762) and of Harvard's Center for Nanoscale Systems, supported by the NSF (ECS-0335765). Some measurements were performed at the National High Magnetic Field Laboratory, which is supported by NSF Cooperative Agreement DMR-1157490 and the State of Florida.

Author contributions

J.D.S.-Y. and J.Y.L. fabricated the samples, performed the transport experiments, analysed the data and wrote the paper. A.F.Y. and B.M.H. performed the capacitance measurements and contributed to the discussion of the results. T.T. and K.W. grew the crystals of hexagonal boron nitride. R.C.A. advised on the capacitance measurements and contributed to the discussion of the results. P.J.-H. advised on the transport experiments, data analysis and writing of the paper.

Additional information

Supplementary information is available in the online version of the paper. Reprints and permissions information is available online at www.nature.com/reprints. Correspondence and requests for materials should be addressed to P.J.H.

Competing financial interests

The authors declare no competing financial interests.

Methods

All studied devices consist of two monolayer graphene flakes stacked together using a dry transfer process[34,35]. The stacking naturally results in a rotational misalignment, or twist, between the layers. We fabricated dual-gated structures where the twisted bilayer was encapsulated by hexagonal boron nitride (hBN) dielectric layers. The hBN also shields the graphene layers from contamination during the fabrication process, resulting in a more homogenous electronic system[34,36]. For the device discussed in the main text, the twisted bilayer was contacted using graphite electrodes, which makes good contact to both layers of the bilayer, even at high magnetic fields (further details in Supplementary Materials). Unless otherwise noted, all measurements were performed in a He3 cryostat at 0.3 K.

References

34. Wang, L. *et al.* One-dimensional electrical contact to a two-dimensional material. *Science* **342,** 614–617 (2013).
35. Zomer, P. J., Guimarães, M. H. D., Brant, J. C., Tombros, N. & van Wees, B. J. Fast pick up technique for high quality heterostructures of bilayer graphene and hexagonal boron nitride. *Appl. Phys. Lett.* **105,** 013101 (2014).
36. Mayorov, A. S. *et al.* Micrometer-scale ballistic transport in encapsulated graphene at room temperature. *Nano Lett.* **11,** 2396–2399 (2011).